

Reconstruction of boosted and resolved multi-Higgs-boson events with symmetry-preserving attention networks

Haoyang Li,^a Marko Stamenkovic,^b Alexander Shmakov,^c Michael Fenton,^c Darius Shih-Chieh Chao,^a Kaitlyn Maiya White,^a Caden Mikkelsen,^d Jovan Mitić,^e Cristina Mantilla Suarez,^f Melissa Quinnan,^a Greg Landsberg,^b Harvey Newman,^d Pierre Baldi,^c Daniel Whiteson,^c and Javier Duarte^a

^aUC San Diego, La Jolla, CA, USA

^bBrown University, Providence, RI, USA

^cUC Irvine, Irvine, CA, USA

^dCaltech, Pasadena, CA, USA

^eUniversity of Belgrade, Belgrade, Serbia

^fUniversity of Virginia, VA, USA

E-mail: marko_stamenkovic@brown.edu

ABSTRACT: The production of multiple Higgs bosons at the CERN LHC provides a direct way to measure the trilinear and quartic Higgs self-interaction strengths as well as potential access to beyond the standard model effects that can enhance production at large transverse momentum p_T . The largest event fraction arises from the fully hadronic final state in which every Higgs boson decays to a bottom quark-antiquark pair ($b\bar{b}$). This introduces a combinatorial challenge known as the *jet assignment problem*: assigning jets to sets representing Higgs boson candidates. Symmetry-preserving attention networks (SPA-Nets) have been developed to address this challenge. However, the complexity of jet assignment increases when simultaneously considering both $H \rightarrow b\bar{b}$ reconstruction possibilities, i.e., two “resolved” small-radius jets each containing a shower initiated by a b quark or one “boosted” large-radius jet containing a merged shower initiated by a $b\bar{b}$ pair. The latter improves the reconstruction efficiency at high p_T . In this work, we introduce a generalization to the SPA-Net approach to simultaneously consider both boosted and resolved reconstruction possibilities and unambiguously interpret an event as “fully resolved,” “fully boosted,” or in between. We report the performance of baseline methods, the original SPA-Net approach, and our generalized version on nonresonant HH and HHH production at the LHC. Considering both boosted and resolved topologies, our SPA-Net approach increases the Higgs boson reconstruction purity by 57–62% and the efficiency by 23–38% compared to the baseline method depending on the final state.

Contents

1	Introduction	1
2	Dataset and Labeling	3
3	Methods	5
3.1	Baseline	5
3.2	SPA-Net	6
3.3	Target Higgs Boson Mass Reweighting	8
4	Postprocessing	9
5	Results	10
5.1	HHH Resolved Training	10
5.2	HHH Boosted+Resolved Training	12
5.2.1	Mass Sculpting	12
5.3	HH Resolved and Boosted+Resolved Trainings	13
6	Summary	13

1 Introduction

Measuring multiple Higgs boson production at the LHC is a powerful probe of the Higgs trilinear (λ_3) and quartic (λ_4) self-couplings as well as new physics effects beyond the standard model (SM), such as resonant production via a heavy particle decaying into two Higgs bosons. While the quartic coupling is challenging to measure at the LHC and requires future colliders to observe the corresponding signature of triple Higgs boson production [1–3], the trilinear coupling can be directly accessed by studying Higgs boson pair production at the LHC. These processes can also exhibit modified kinematics and enhanced cross sections at large transverse momentum p_T for non-SM coupling values [4–9]. The dominant decay mode of the Higgs boson is into a bottom quark-antiquark ($b\bar{b}$) pair, which leads to a fully hadronic final state with multiple jets. Representative Feynman diagrams for the production of two or three Higgs bosons in the gluon-gluon fusion process where all Higgs bosons decay to $b\bar{b}$ pairs are shown in Fig. 1. A key challenge in this final state is to find the optimal association of jets to Higgs boson candidates. This problem is combinatorial in nature and becomes computationally challenging for conventional methods as the number of jets increases.

Moreover, the complexity of this problem is further increased by the presence of different event topologies, depending on the p_T of the Higgs bosons. At low p_T , each Higgs

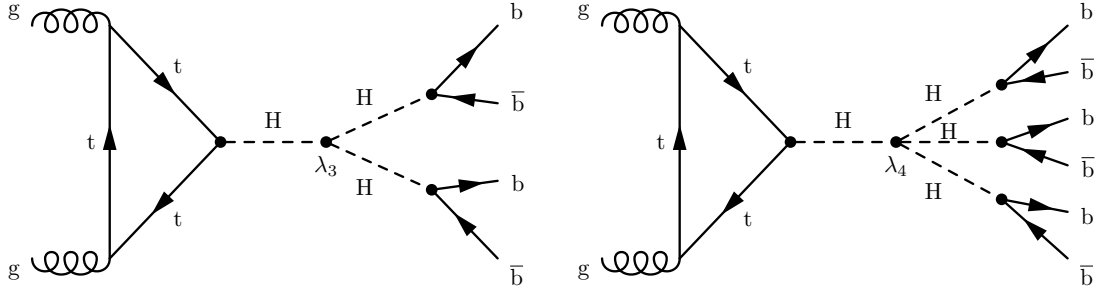


Figure 1: Representative Feynman diagrams for the production of two Higgs bosons (left) and three Higgs bosons (right) in the gluon-gluon fusion process, where all Higgs bosons decay to $b\bar{b}$ pairs.

boson can be reconstructed as two “resolved” small-radius jets, each containing a b-quark-initiated jet. At high p_T , each Higgs boson can be reconstructed from one “boosted” large-radius jet, containing a merged $b\bar{b}$ pair. For intermediate p_T , a mixture of resolved and boosted jets can be present. This is illustrated in Fig. 2 The CMS and ATLAS Collaborations have performed many searches for resonant and non-resonant Higgs boson pair production in boosted [10, 11] and resolved [12–15] final states, and their statistical combination [16–22]. The combination of these two channels is challenging because the two data samples need to be statistically independent, but the two selection criteria can often select the same events, especially for Higgs bosons in the intermediate p_T range. Thus, analysts must implement an “overlap removal” procedure to allow these two searches to be combined. Part of the motivation of this work is to use machine learning to help interpret individual events as either boosted or resolved.

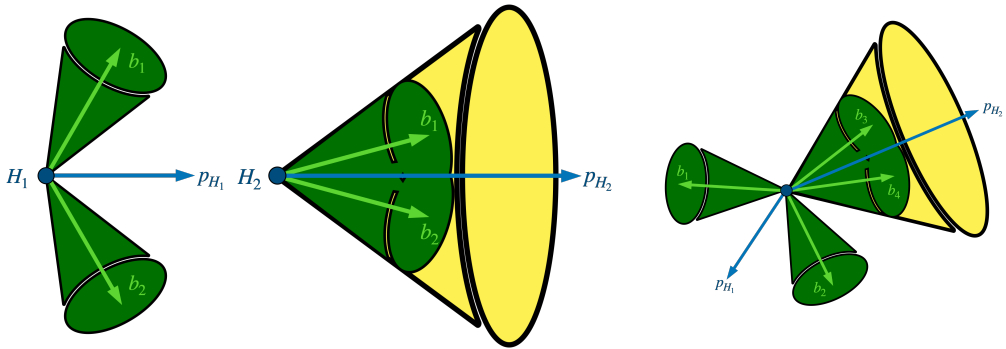


Figure 2: Two bottom quarks from a Higgs boson decay are reconstructed as two separated small- R jets in the resolved topology when the Higgs boson $p_T \lesssim 2m_H/R$ (left). Two bottom quarks from a Higgs boson decay overlap and merge into a single large- R jet in the boosted topology when the Higgs boson $p_T \gtrsim 2m_H/R$ (center). An event with two Higgs bosons where one is resolved and one is boosted (right)

Symmetry-preserving attention networks (SPA-Nets) are a novel class of neural networks that have been proposed [23–25] to solve the jet assignment problem for a fixed event topology. They have also been studied in the context of resolved nonresonant HH events to improve the sensitivity to λ_3 at the high-luminosity LHC [26]. In this work, we present a generalization of the SPA-Net approach to handle variable (boosted and resolved) event topologies and simultaneously consider both small- and large-radius jets. We apply this approach to nonresonant HH and HHH production at the LHC and compare its performance with baseline methods and the original fully resolved SPA-Net approach. Finally, we also demonstrate how SPA-Net can provide a partitioning of events into disjoint categories based on the number of reconstructed boosted Higgs boson candidates.

The rest of this paper is organized as follows. Section 2 presents the dataset and ground truth labeling. We describe the baseline methods and SPA-Net model configurations in Section 3. In Section 4, we delineate how we use the SPA-Net outputs to assign jets and categorize events. We present the results in Section 5 and summarize in Section 6.

The dataset [27] and code [28] for analyzing it are publicly available. For implementing the training, we use the SPANET library version 2.2 with additions related to reweighting and an improved validation accuracy metric described in Section 3 in a custom fork on GitHub [29].

2 Dataset and Labeling

Nonresonant HH and HHH events are generated using MADGRAPH5_aMC@NLO3.4.1 [30] at the LHC with a center of mass energy $\sqrt{s} = 14$ TeV, with the trilinear and quartic couplings fixed to the SM values as implemented in the model of Ref. [31]. Only the decay of the Higgs boson to bottom quarks is considered. The parton shower and hadronization are simulated with PYTHIA8.2 [32] and the detector response is simulated with DELPHES3.4.1 [33], using the CMS parametrization.

Final-state particles are clustered into jets using the anti- k_T algorithm [34, 35] with radius parameters of 0.5 (AK5 jets) and 0.8 (AK8 jets). We require $p_T > 20$ GeV for AK5 jets and $p_T > 200$ GeV for AK8 jets, as well as $|\eta| < 2.5$ for both. Emulation of a b-tagging algorithm is applied to the AK5 jets, which assigns a boolean value to each jet indicating whether it originates from a b quark, based on p_T -dependent efficiency and misidentification rates. The misidentification rate for light (c) jets is about 1% (20%), while the b-tagging efficiency is about 70% [36]. We note that these are conservative relative to current state-of-the-art b-tagging algorithms [37]. The four-momentum (p_T, η, ϕ, m) and the b-tagging value of each AK5 jet are stored as inputs to the networks. For AK8 jets, we consider the four-momentum (p_T, η, ϕ, m) as well. No b-tagging is applied for AK8 jets, however, we develop our own tagger discussed in Section 3.1.

The ground truth assignments are obtained by matching the reconstructed jets to the simulated b quarks from the Monte Carlo event record, using a distance measure $\Delta R = \sqrt{\Delta\phi^2 + \Delta\eta^2}$. For AK5 jets, $\Delta R < 0.5$ is required between each jet and b quark daughter, and a pair of jets is labeled as a true Higgs boson if they match to the same Higgs boson in the event record. For AK8 jets, the jet is labeled a true Higgs boson if

$\Delta R < 0.8$ between the jet and the Higgs boson, and between the jet and both b quark daughters. Multiple Higgs boson candidates are allowed in both reconstructions. The truth-level matching efficiency of Higgs boson candidates as a function of their p_T is shown in Fig. 3. For $p_T > 400$ GeV, AK8 jets have a higher matching efficiency than AK5 jets. No overlap removal is performed at this stage.

HHH events that contain at least six AK5 jets are selected, while HH events are selected if they contain at least four AK5 jets. Up to ten AK5 jets and three AK8 jets are considered for both event types. No b-tagging requirements are applied. Approximately 0.8 million HHH events and 1.2 million HH events pass this pre-selection. These events are split as follows: 90.25% for training the resolved SPA-Net, 4.75% for validation and hyper-parameter optimization, and 5% for testing.

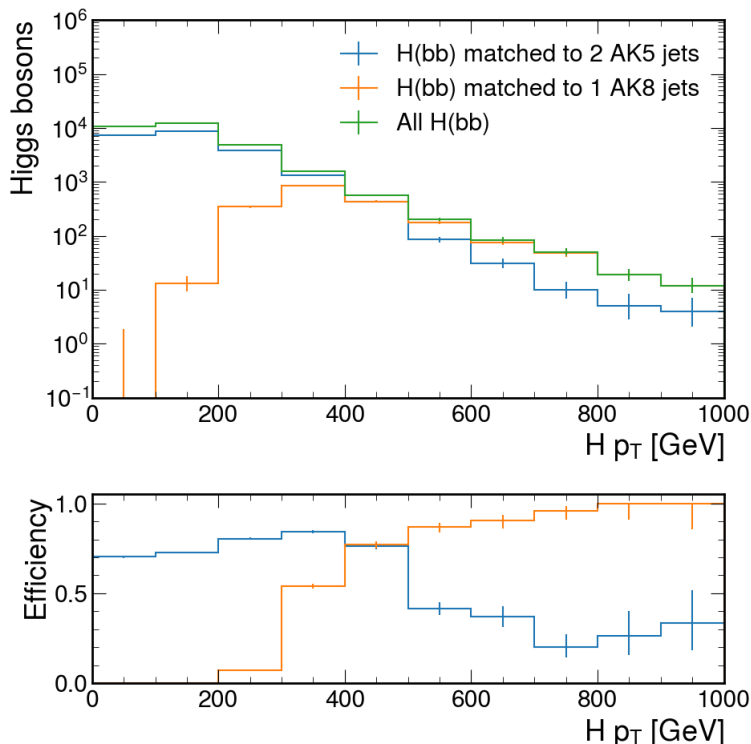


Figure 3: Reconstruction efficiency for true Higgs bosons to be reconstructed and matched to either two AK5 jets or one AK8 jet as a function of p_T in HHH events.

To evaluate any potential distortions in the mass distribution, known as *mass sculpting*, we doubled the SM HHH dataset and increased the SM HHH training+validation dataset by simulating additional nonresonant HHH events with Higgs boson masses set to 120, 122.5, 127.5, and 130 GeV. Each additional mass point contains the same number of events with the SM HHH training and validation dataset before pre-selection. These datasets were combined prior to training the boosted+resolved HHH SPA-Net models. This approach aims to produce a flatter Higgs boson mass distribution and reduce mass sculpting effects.

Sample	N_{events}	Training Fraction	Validation Fraction	Testing Fraction
HHH, $m_H = 125$ GeV	855,254	90.25%	4.75%	5%
HHH, $m_H \in \{120, 122.5, 125, 127.5, 130\}$ GeV	9,580,718	95%	5%	—
HH, $m_H = 125$ GeV	1,209,807	90.25%	4.75%	5%
QCD multijet	127,876	80%	—	20%

Table 1: The number of events N_{events} after pre-selection. Since this study focuses exclusively on SPA-Net’s performance on SM signals and backgrounds, we evaluated SPA-Net only on the SM testing dataset ($m_H = 125$ GeV). Consequently, the testing fraction of the HHH dataset, including non-SM mass points, is not applicable. The QCD dataset was used to train the BDT baseline introduced in Section 3.1 and test the mass sculpting effect of the SPA-Net models and the baselines. No validation fraction was allocated for the QCD dataset, as we did not perform hyperparameter tuning for the BDT.

We also generated a background dataset from events composed uniquely of jets produced through the strong interaction, referred to as quantum chromodynamics (QCD) multijet events, using the same generator as for the non-resonant HH and HHH events. To ensure a sufficient sample size with real high- p_T b jets, we generated 4 b partons and required their scalar p_T sum to be $H_T > 250$ GeV. After applying the same pre-selection criteria as for the HHH events, the QCD test dataset consists of approximately 25,000 events.

A summary of the dataset used in this study is shown Table 1.

3 Methods

3.1 Baseline

The resolved training of SPA-Net is benchmarked against the χ^2 method [38], which minimizes the following quantity:

$$\chi^2 = (m(j_a, j_b) - m_H)^2 + (m(j_c, j_d) - m_H)^2 + (m(j_e, j_f) - m_H)^2, \quad (3.1)$$

where $m(j_a, j_b)$ is the invariant mass of a pair of AK5 jets j_a and j_b and $m_H = 125$ GeV is the nominal mass of the Higgs boson. The AK5 jets are sorted in descending order by p_T , with the b-tagged sorted jets coming first and the non-b-tagged coming last. For the χ^2 method, only the first six jets are considered.

For the boosted topology baseline, the DELPHES configuration lacks a parameterized boosted Higgs boson AK8 jet tagger in DELPHES, so we train a boosted decision tree (BDT) tagger as a baseline to compare with SPA-Net. Given an AK8 jet, the BDT input variables are the p_T , η , mass m , soft-drop mass m_{SD} [39], fraction of charged energy, number of charged particles, and the N -subjettiness jet substructure variables τ_{32} and τ_{21} [40]. The BDT output score represents the probability that the AK8 jet is an $H \rightarrow b\bar{b}$ jet rather than a QCD jet. It was trained on a dataset that combined the AK8 jets in the SM HHH training set and the AK8 jets in the QCD training set, which consists of 164,601 $H \rightarrow b\bar{b}$ jets and 553,548 QCD jets. The classes were balanced during training.

3.2 SPA-Net

SPA-Net [23–25] is a general attention-based neural network architecture for the assignment of reconstructed physics objects (e.g., jets or leptons) to truth-level particles (e.g., Higgs bosons or top quarks). Since its introduction, there have been several improvements that we leverage in this paper.

The structure of SPA-Net, shown in Fig. 4, consists of five distinct components:

- (1) independent object embeddings to produce latent space representations for each reconstructed object;
- (2) a central stack of transformer encoders;
- (3) additional transformer encoders for each target;
- (4) a tensor-attention to produce the object-target assignment distributions; and
- (5) a classification head for target detection.

The transformer encoders employ multi-head self-attention [41] with one significant modification: the positional embeddings are combined with *position-independent* physics object embeddings which preserve permutation invariance in the input.

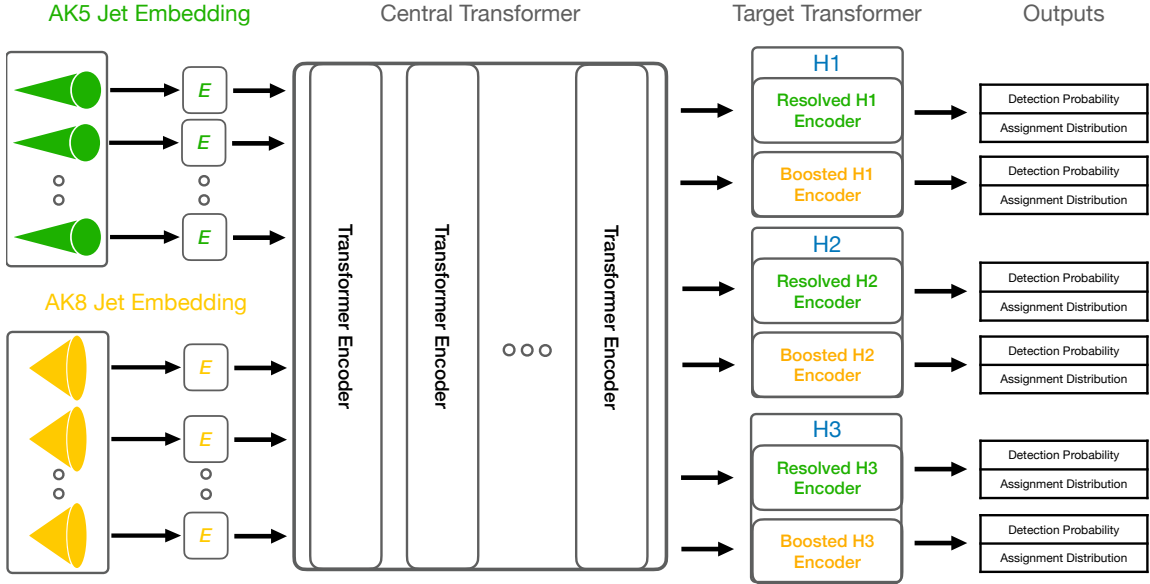


Figure 4: Diagram of the SPA-Net architecture used in this work for HHH events. Both large-radius (AK8) and small-radius (AK5) jets are input to the model with separate Higgs boson targets. The resolved Higgs boson targets consist of pairs of AK5 jets, while the boosted Higgs boson targets consist of single AK8 jets.

While the original SPA-Net studies concentrated on examples where all physics objects were of the same type (e.g., small-radius jets), it was updated in Ref. [25] to allow for the consideration of different types of physics objects, specifically leptons. In this application,

we leverage this improvement with the novelty of considering both small-radius and large-radius jets, which may both be associated to the same truth-particle.

We accommodate these additional inputs by training individual position-independent embeddings for each *class* of input. This allows the network to adjust to the various distributions for each input type, and allows us to define sets of features specific to each type of object. The individual embedding layers map these disparate objects with different features into a unified latent space, which may be processed by the central transformer. The encoded event vector after the central transformer is a latent summary representation of the entire event.

Depending on its transverse momentum, a Higgs boson can be reconstructed in a resolved topology, meaning two AK5 jets, or a boosted topology, meaning a single AK8 jet. Moreover, these two possibilities are not mutually exclusive in that a single Higgs boson may be reconstructible in both ways. Motivated by the two different topologies, we replaced the particle transformer branches in the original SPA-Net [23, 24] by target transformer branches to enable the same particle to be reconstructed in two different classes of objects. To account for the two possible topologies for each particle, we designed a resolved target and a boosted target for each potential Higgs boson in an event. Each target’s branch follows the same architecture as the “particle” branch illustrated in Ref. [23] and includes a tensor attention output and a binary detection output.

The tensor attention output is interpreted as the assignment probability (AP). Each entry of the tensor represents the likelihood that a set of objects reconstructs the target. The indices of the tensor entry indicate which objects are to be assigned to the target. The assignment outputs are trained only on examples in which the event contains all detector objects necessary for a correct target assignment, i.e. the target is *reconstructible*. Nonreconstructible targets are ignored via the masked loss defined in Eq. (6) of Ref. [24]. As a result, the SPA-Net *assignment probability* only represents a conditional assignment distribution over jet indices for each target given that the target is reconstructible.

Since Ref. [24] introduced the ability to reconstruct partial events, it is important to estimate the probability that a given target is reconstructible in the event. This *detection probability* is estimated with an additional output head of SPA-Net. Specifically, a summary *target vector* is extracted from each of the target transformer encoders. These target vectors are fed into a feedforward binary classification network to produce a detection probability for each target. We also take into account the event-level symmetries in a similar manner to the assignment reconstruction loss from Eq. (6) of Ref. [24]. This detection output is trained with a cross-entropy loss over the symmetric target masks.

The complete loss equation for the entire network is given by

$$\mathcal{L} = \alpha_0 \mathcal{L}_{\text{assignment}} + \alpha_1 \mathcal{L}_{\text{detection}}, \quad (3.2)$$

where α_0 and α_1 are the weights of the different components of the loss function. In this work, we use $\alpha_0 = 20$ and $\alpha_1 = 1$.

3.3 Target Higgs Boson Mass Reweighting

The mass distribution of the resolved and boosted Higgs boson targets in the combined HHH dataset is shown in Fig. 5 (left). Despite varying the Higgs boson mass between 120 and 130 GeV, both the resolved and boosted targets still possess an obvious peak around $m_H = 125$ GeV. An overabundance of samples at $m_H = 125$ GeV in the training set could bias the SPA-Net algorithm to reconstruct Higgs bosons by simply choosing the jet assignment where the invariant mass is closest to $m_H = 125$ GeV. This behavior is undesirable because a reconstruction that heavily relies on the invariant mass can result in *mass sculpting* of the background, that is introducing an artificial signal-like peak in the invariant mass distribution even when no signal is present.

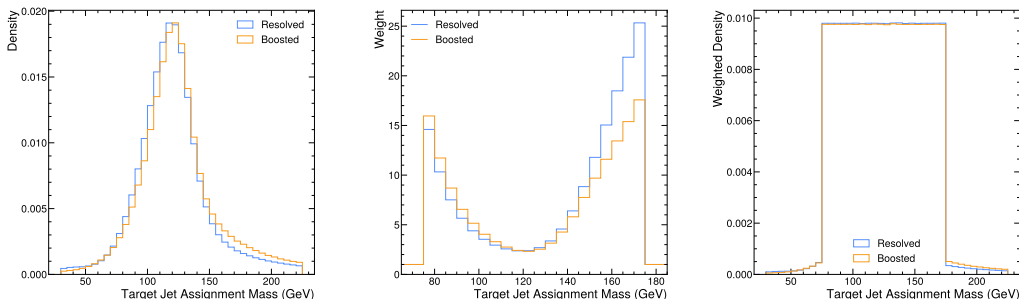


Figure 5: The mass distributions of target jet assignments show peak-like shapes, despite the Higgs targets being generated at uniformly spaced mass points (left). The weights derived to flatten the mass spectrum in the range $m \in [75, 175]$ GeV (center). Outside the mass range $[75, 175]$ GeV, the weights are one. The resulting mass distribution after reweighting (right).

To further prevent SPA-Net from reconstructing Higgs bosons only based on the invariant mass of the jet assignment, we implemented a binned reweighting as a function of the Higgs boson target mass $m \in [75, 175]$ GeV. The weights were calculated independently for each topology and were incorporated in the loss term calculation. For each topology and each mass bin of width 5 GeV, we calculated the weight as

$$w(m) = \begin{cases} \frac{p_{\text{uniform}}(m_i)}{p_{\text{mass}}(m_i)}, & 75 \leq m_i \leq m < m_{i+1} \leq 175 \text{ GeV} \\ 1, & m \notin [75, 175] \text{ GeV} \end{cases}, \quad (3.3)$$

where p_{mass} is the real mass distribution and p_{uniform} is the desired uniform distribution, and m_i and m_{i+1} are bin edges. The calculated weight for each bin for each topology is shown in Fig. 5 (center). We assigned a weight of one to the targets outside the mass range $[75, 175]$ GeV to prevent assigning a high weight to outliers. The weights are incorporated into the calculations for both the assignment loss and the detection loss. For instance, the

assignment loss is modified as follows,

$$\mathcal{L}_{\text{assignment}} = \min_{\sigma \in G_t} \sum_{i=1}^{N_{\text{target}}} w_{\sigma(i)} \text{CCE}(P_i, T_{\sigma(i)}), \quad (3.4)$$

where CCE represents the categorical cross-entropy loss, G_t denotes the permutation group of all targets, σ is an element of the permutation group, N_{target} represents the maximum number of the targets that the SPA-Net model can output, P_i is the i th predicted jet assignment, $T_{\sigma(i)}$ is the i th target jet assignment under permutation σ , and $w_{\sigma(i)}$ is the calculated weight associated with $T_{\sigma(i)}$. Equation (3.4) can also be applied to the detection loss by replacing the categorical cross-entropy loss with the binary cross-entropy loss.

The target weights were also integrated into the validation metrics. During training, the best checkpoint was selected based on the weighted jet assignment accuracy (JA), averaged across the events in the validation dataset. JA is defined as

$$\text{JA} = \frac{1}{\sum_{i=1}^{N_{\text{target}}} w_i} \max_{\sigma \in G_t} \sum_{i=1}^{N_{\text{target}}} w_{\sigma(i)} [P_i \equiv T_{\sigma(i)}], \quad (3.5)$$

where $[x \equiv y]$ represents a function that outputs 1 if the jet assignments x and y are equivalent, and 0 otherwise. Another key difference between our validation metric and the default SPA-Net validation metric lies in the selection of events used for the computation. The default SPA-Net validation accuracy is averaged only across events in which all possible target particles are reconstructible (fully reconstructible events). However, we found that we needed to include partially reconstructible events as well when incorporating boosted and resolved targets because only a small fraction of events contain three Higgs bosons that can be reconstructed in both topologies.

4 Postprocessing

We postprocess the outputs for the two topologies separately. For each topology, we calculate the most probable number of Higgs bosons in that topology based on the multinomial distribution. Here, DP_i represents the detection probability of the i th Higgs boson in a given topology of HHH events. Using a threshold of 0.5, we consider the i th Higgs boson to be detected if DP_i is greater than or equal to 0.5. The corresponding probabilities for detecting a specific number of Higgs bosons, N_{H} , are then calculated as:

$$p(N_{\text{H}} = 0) = (1 - \text{DP}_1)(1 - \text{DP}_2)(1 - \text{DP}_3) \quad (4.1)$$

$$\begin{aligned} p(N_{\text{H}} = 1) &= \text{DP}_1(1 - \text{DP}_2)(1 - \text{DP}_3) \\ &\quad + \text{DP}_2(1 - \text{DP}_1)(1 - \text{DP}_3) \\ &\quad + \text{DP}_3(1 - \text{DP}_1)(1 - \text{DP}_2) \end{aligned} \quad (4.2)$$

$$p(N_{\text{H}} = 2) = \text{DP}_1\text{DP}_2(1 - \text{DP}_3) + \text{DP}_2\text{DP}_3(1 - \text{DP}_1) + \text{DP}_3\text{DP}_1(1 - \text{DP}_2) \quad (4.3)$$

$$p(N_{\text{H}} = 3) = \text{DP}_1\text{DP}_2\text{DP}_3. \quad (4.4)$$

Then, we obtain the most probable number of Higgs bosons in the topology, \hat{N}_H , as

$$\hat{N}_H = \arg \max_{N_H} p(N_H), \quad (4.5)$$

Subsequently, we select the top \hat{N}_H Higgs boson’s jet assignments ranked by the product $DP_i AP_i$, which combines the detection probability (whether the Higgs boson exists in this topology) with the assignment probability (the confidence of the jet assignment) to prioritize the most reliable candidates.

Additionally, to accurately analyze Higgs bosons originating from both resolved and boosted topologies, it is crucial to implement strategies that prevent double counting. Without such measures, the same Higgs boson could be reconstructed in both topologies and appear twice in different categories. In this study, we address this issue by prioritizing boosted Higgs boson candidates as those have a significantly better signal-to-background ratio. Specifically, resolved Higgs boson candidates are discarded if any of their associated AK5 jets overlap with boosted candidates. The overlap condition was defined using a separation criterion of $\Delta R < 0.5$.

5 Results

The algorithm’s performance is quantified using two metrics: *reconstruction efficiency* and *reconstruction purity*. Reconstruction efficiency refers to the fraction of target Higgs bosons that are correctly reconstructed by the SPA-Net jet assignment. Conversely, reconstruction purity is defined as the fraction of reconstructed Higgs bosons that match the target Higgs bosons. Here, the matching condition requires that the candidate and target Higgs bosons have the same jet assignment. These metrics are computed per particle target, rather than at the event level.

In this section, we present results for the following SPA-Net trainings:

1. HHH events targeting (a) a resolved-only topology considering up to 10 AK5 jets and (b) resolved and boosted topologies, the latter considering up to 3 AK8 jets.
2. HH events targeting (a) a resolved-only topology considering up to 10 AK5 jets and (b) resolved and boosted topologies, the latter considering up to 2 AK8 jets.

The training configurations are shown in Table 2.

5.1 HHH Resolved Training

Figure 6 presents the Higgs reconstruction purity and efficiency as functions of the Higgs boson candidate transverse momentum p_T for the fully resolved SPA-Net training. Below $p_T < 600$ GeV, SPA-Net demonstrates a higher reconstruction efficiency than the χ^2 baseline, except in the first bin.

As described in Section 4, we discard jet assignments where $\hat{N}_H < 3$, which indicates that not all Higgs bosons could be reconstructed. This procedure aims to balance reconstruction purity and efficiency and results in enhanced reconstruction purity with respect

Table 2: The training configurations of the models presented in Section 5 are described.

Parameter	Benchmark Models			
	HHH Boosted+Resolved	HHH Resolved	HH Boosted+Resolved	HH Resolved
Training Epochs	500	500	4000	4000
Learning Rate	0.0005	0.0005	0.0015	0.0015
Batch Size	4096	4096	4096	4096
Dropout	0.2	0.2	0.2	0.2
L2 Gradient Clipping	1.0	1.0	1.0	1.0
L2 penalty	0.0002	0.0002	0.0002	0.0002
Hidden Dimension	64	64	32	32
Central Encoders	8	8	8	8
Branch Encoders	6	6	6	6
Partial Event Training	Yes	Yes	Yes	Yes
Cosine Annealing Cycles	5	5	1	1

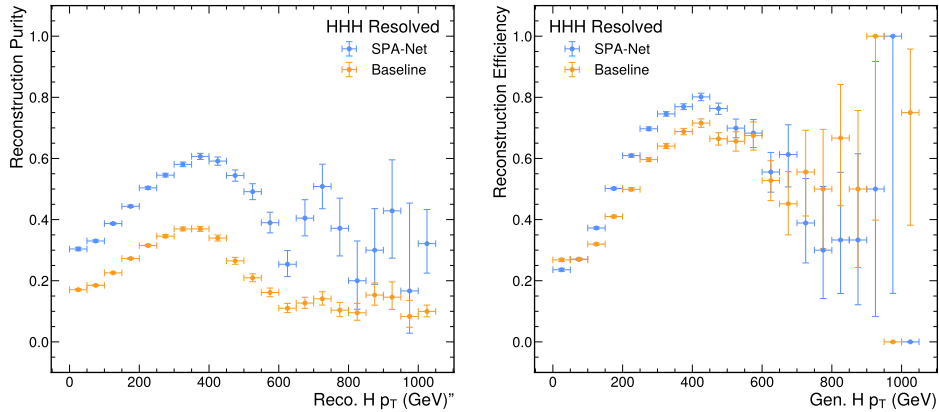


Figure 6: On the left, Reco. H refers to the Higgs boson candidates reconstructed by the SPA-Net jet assignments. The reconstruction purity is defined as the fraction of the Higgs boson candidates that have the same jet assignment as the target. On the right, Gen. H refers to the Higgs boson targets consisting of the target jet assignments. The reconstruction efficiency is defined as the fraction of the target Higgs bosons recovered by the SPA-Net predictions. The error bar in each bin is the Clopper-Pearson interval.

to the baseline, as shown in Fig. 6. However, this balancing strategy can occasionally discard valid jet assignments, reducing the reconstruction efficiency. For analyses prioritizing reconstruction efficiency, the DP threshold (effectively set to 0.5 in this study) could be lowered to retain more jet assignments, albeit at the cost of reduced reconstruction purity.

The jet assignment performance is affected by the angular separation of the two jets from the Higgs boson decay, which depends on the Higgs boson momentum. For low p_T , the jets are widely separated and distributed across the detector, making the jet assignment challenging for three Higgs bosons. For high p_T , the jets are more collimated and the jet correlation is more evident. However, above $p_T > 400$ GeV, the efficiency drops due to the increased probability of merging two jets into a large-radius jet or losing one of the b

jets out of the detector acceptance. This limitation can be overcome by incorporating the large-radius AK8 jets in the SPA-Net training.

5.2 HHH Boosted+Resolved Training

Figure 7 shows the Higgs reconstruction purity and efficiency versus the Higgs boson candidate transverse momentum p_T for the SPA-Net model trained on both resolved and boosted targets. Compared with Fig. 6, the boosted+resolved SPA-Net exhibits significantly better performance above $p_T > 400$ GeV as a result of including boosted targets in the training.

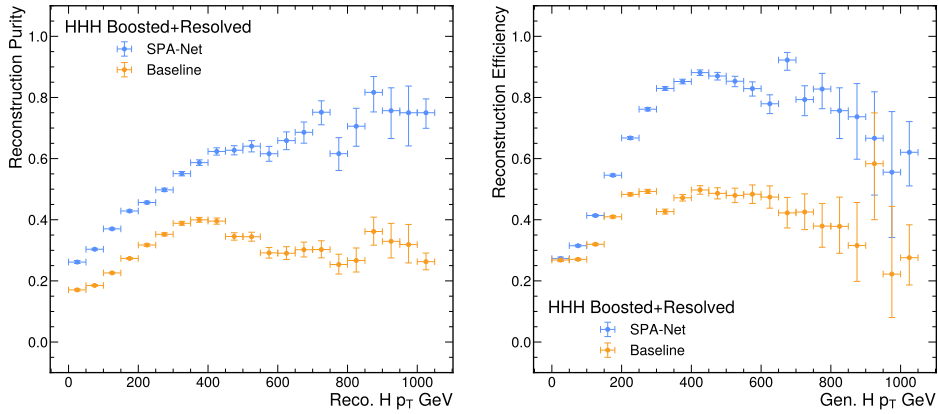


Figure 7: SPA-Net’s performance improves in the high- p_T region when boosted targets are incorporated during training. A comparison of boosted+resolved SPA-Net with the χ^2 +BDT baseline shows that SPA-Net consistently outperforms the baseline across both evaluation metrics. The axis definitions are the same as those in Fig. 6.

As introduced in Section 3.1, the baseline utilizes the χ^2 method to assign AK5 jets to resolved Higgs boson targets and applies the BDT to classify AK8 jets into boosted Higgs boson candidates or background. Similar to SPA-Net, which predicts and reconstructs candidates in both topologies for each event, the χ^2 -based resolved baseline and the BDT-based boosted baseline also operate on each event. In this study, we assume the χ^2 baseline always predicted three resolved Higgs boson candidates in the resolved topology. For the boosted topology, we select the AK8 jets of which BDT scores passing the loose working point of 0.911348, corresponding to a background misidentification rate of 2%. Finally, the Higgs boson candidates predicted by both baselines undergo the same overlap-removal procedure in Section 4.

Across all Higgs boson p_T bins, the boosted+resolved SPA-Net exhibits higher Higgs boson reconstruction purity and efficiency than the χ^2 and BDT baseline.

5.2.1 Mass Sculpting

As specified at the end of Section 2, the training dataset of the boosted+resolved SPA-Net includes Higgs bosons simulated at mass points different than 125 GeV. We ran inference of the boosted+resolved SPA-Net model on the QCD test dataset introduced in

Section 2. Figure 8 shows the mass distribution of the Higgs boson candidates predicted by the boosted+resolved SPA-Net model is smoother and does not peak at 125 GeV compared to that of the χ^2 +BDT baseline, indicating the boosted+resolved SPA-Net model distorts the mass distribution less than the baseline.

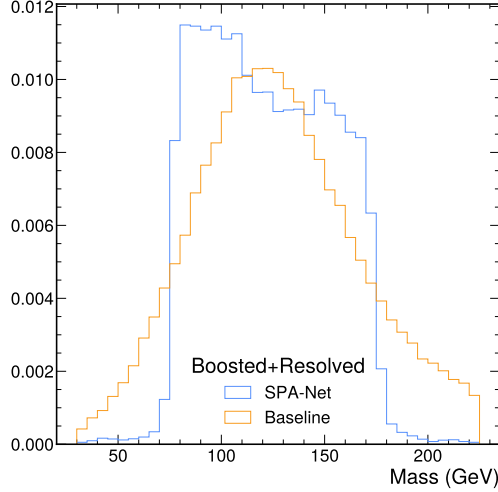


Figure 8: The boosted+resolved SPA-Net model, trained with the calculated weights, outperforms the χ^2 +BDT baseline in reducing the correlation between the jet assignments and the reconstructed Higgs boson candidate mass.

5.3 HH Resolved and Boosted+Resolved Trainings

As $HH \rightarrow 4b$ events are more likely to be detected at the LHC, we trained one SPA-Net using HH resolved targets and another using both HH boosted and resolved boosted targets. We then evaluate their Higgs boson reconstruction purity and efficiency. The corresponding Higgs boson reconstruction results are shown in Figs. 9 and 10, respectively.

Similar to the HHH results, the HH results demonstrate that SPA-Net achieves higher Higgs boson reconstruction purity and efficiency than the baseline, modified to target two reconstructed Higgs bosons with the first four jets ranked in Section 3.1, across all p_T bins. Furthermore, the comparison between the resolved SPA-Net and the boosted+resolved SPA-Net shows that incorporating boosted Higgs boson targets can enhance SPA-Net’s Higgs boson reconstruction purity and efficiency for $p_T > 400$ GeV.

6 Summary

We adapted the enhanced symmetry-preserving attention network (SPA-Net) to reconstruct multiple Higgs bosons in HHH and HH events, addressing both resolved and boosted topologies. Our HHH boosted+resolved SPA-Net training demonstrated superior Higgs boson reconstruction purity and efficiency compared to a baseline approach combining a

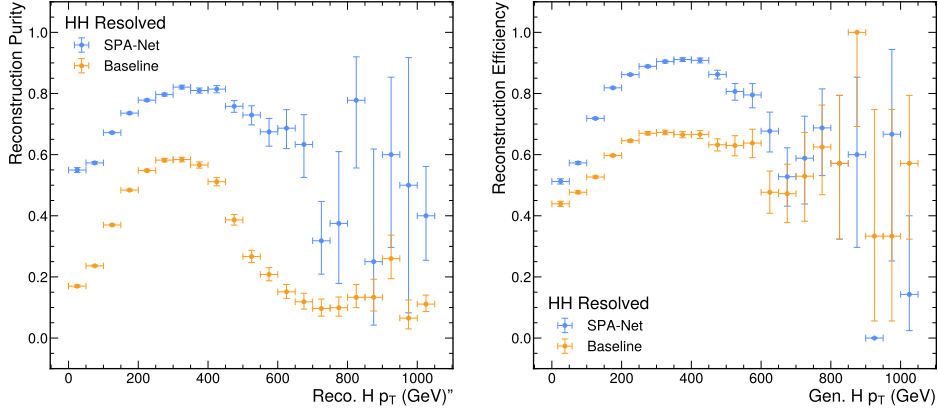


Figure 9: Our resolved SPA-Net trained on HH targets consistently outperforms the χ^2 baseline across both evaluation metrics. The axis definitions are the same as those in Fig. 6.

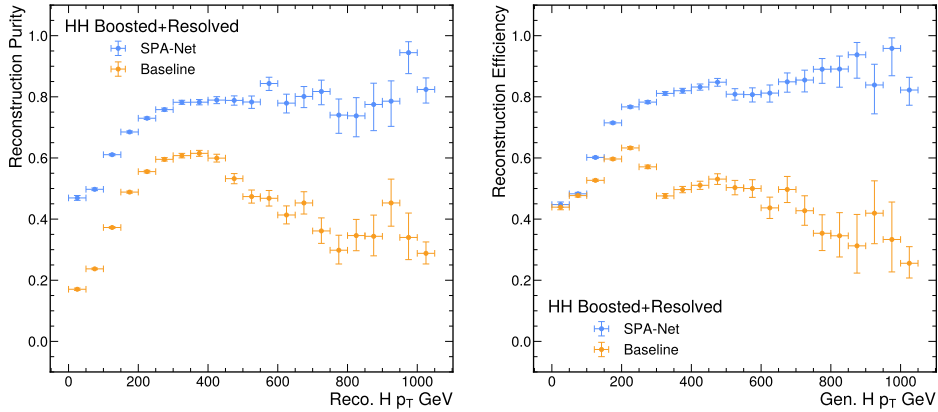


Figure 10: Similarly, compared to Figure 9, SPA-Net’s performance improves in the high- p_T region when boosted targets are incorporated during training. A comparison of boosted+resolved SPA-Net training with the χ^2 +BDT baseline shows that SPA-Net consistently outperforms the baseline across both evaluation metrics. The axis definitions are the same as those in Fig. 6.

χ^2 -based methods and a boosted decision tree (BDT) large-radius jet tagger, as shown in Table 3. In particular, for HHH (HH) events considering both boosted and resolved topologies, our SPA-Net approach increases the H purity by 57% (62%) and the H efficiency by 38% (23%) compared to the baseline method.

To assess mass sculpting effects, we applied the boosted+resolved SPA-Net to a background multijet dataset and observed a less pronounced peak-like distribution compared to the baseline. Furthermore, we extended the boosted+resolved SPA-Net to HH events, where it similarly outperformed the χ^2 +BDT baseline. Notably, in the high- p_T region,

Table 3: Summary of overall Higgs boson reconstruction purity and efficiency for the models discussed in Section 5. The row “Reco. Target H ” indicates the number of target Higgs bosons successfully recovered by each model. Most models show a decline in Reco. Target H when transitioning from the resolved dataset to the boosted+resolved dataset, except for the HHH SPA-Net. This decline is attributed to the overlap removal described in Section 4, where more resolved jet assignments are removed than the number of additional boosted jet assignments included.

Metrics	HHH				HH			
	Resolved		Boosted+Resolved		Resolved		Boosted+Resolved	
	Baseline	SPA-Net	Baseline	SPA-Net	Baseline	SPA-Net	Baseline	SPA-Net
H Purity	0.251	0.430	0.260	0.408	0.390	0.702	0.402	0.651
H Efficiency	0.394	0.448	0.367	0.506	0.578	0.769	0.547	0.674
Reco. Target H	32,223	36,630	30,787	42,457	47,039	62,562	45,481	56,056
Target H	81,810	81,810	83,858	83,858	81,330	81,330	83,178	83,178

incorporating boosted targets in the training led to improved reconstruction purity and efficiency.

In addition, we proposed using predictions of SPA-Net to construct a likelihood for the number of reconstructed boosted and resolved Higgs bosons. By further prioritizing boosted Higgs boson candidates and removing the overlapping resolved Higgs boson candidates, we can uniquely categorize events into boosted or resolved topologies.

Overall, our results show that the boosted+resolved SPA-Net algorithm provides significant improvements in Higgs boson reconstruction across both HHH and HH events, demonstrating its potential as a powerful tool for analyzing multi-Higgs boson final states.

Acknowledgments

This work was supported by the Research Corporation for Science Advancement (RCSA) under grant #CS-CSA-2023-109, Alfred P. Sloan Foundation under grant #FG-2023-20452, U.S. Department of Energy (DOE), Office of Science, Office of High Energy Physics Early Career Research program under Award No. DE-SC0021187, and the U.S. National Science Foundation (NSF) Harnessing the Data Revolution (HDR) Institute for Accelerating AI Algorithms for Data Driven Discovery (A3D3) under Cooperative Agreement PHY-2117997. This work was performed using the Pacific Research Platform Nautilus HyperCluster supported by NSF awards CNS-1730158, ACI-1540112, ACI-1541349, OAC-1826967, the University of California Office of the President, and the University of California San Diego’s California Institute for Telecommunications and Information Technology/Qualcomm Institute. Thanks to CENIC for the 100 Gpbs networks. Part of this research was conducted using computational resources and services at the Center for Computation and Visualization, Brown University.

References

- [1] H. Abouabid et al., HHH *whitepaper*, *Eur. Phys. J. C* **84** (2024) 1183 [2407.03015].

- [2] A. Dainese, M. Mangano, A.B. Meyer, A. Nisati, G. Salam and M.A. Vesterinen, *Report from Working Group 2: Higgs physics at the HL-LHC and HE-LHC*, *CERN Yellow Rep. Monogr.* **7** (2019) 221 [[1902.00134](#)].
- [3] T. Plehn and M. Rauch, *The quartic higgs coupling at hadron colliders*, *Phys. Rev. D* **72** (2005) 053008 [[hep-ph/0507321](#)].
- [4] M.J. Dolan, C. Englert, N. Greiner and M. Spannowsky, *Production of HHjj at the LHC*, *Phys. Rev. Lett.* **112** (2014) 101802 [[1310.1084](#)].
- [5] M.J. Dolan, C. Englert, N. Greiner, K. Nordstrom and M. Spannowsky, *HHjj production at the LHC*, *Eur. Phys. J. C* **75** (2015) 387 [[1506.08008](#)].
- [6] F. Bishara, R. Contino and J. Rojo, *Higgs pair production in vector-boson fusion at the LHC and beyond*, *Eur. Phys. J. C* **77** (2017) 481 [[1611.03860](#)].
- [7] A. Carvalho, M. Dall’Osso, T. Dorigo, F. Goertz, C.A. Gottardo and M. Tosi, *Higgs pair production: Choosing benchmarks with cluster analysis*, *JHEP* **04** (2016) 126 [[1507.02245](#)].
- [8] E. Arganda, C. Garcia-Garcia and M.J. Herrero, *Probing the Higgs self-coupling through double Higgs production in vector boson scattering at the LHC*, *Nucl. Phys. B* **945** (2019) 114687 [[1807.09736](#)].
- [9] M. Capozzi and G. Heinrich, *Exploring anomalous couplings in Higgs boson pair production through shape analysis*, *JHEP* **03** (2020) 091 [[1908.08923](#)].
- [10] CMS collaboration, *Search for production of Higgs boson pairs in the four b quark final state using large-area jets in proton-proton collisions at $\sqrt{s} = 13$ TeV*, *JHEP* **01** (2019) 040 [[1808.01473](#)].
- [11] CMS collaboration, *Search for Nonresonant Pair Production of Highly Energetic Higgs Bosons Decaying to Bottom Quarks*, *Phys. Rev. Lett.* **131** (2023) 041803 [[2205.06667](#)].
- [12] CMS collaboration, *Search for resonant pair production of Higgs bosons decaying to bottom quark-antiquark pairs in proton-proton collisions at 13 TeV*, *JHEP* **08** (2018) 152 [[1806.03548](#)].
- [13] CMS collaboration, *Search for nonresonant Higgs boson pair production in the $b\bar{b}b\bar{b}$ final state at $\sqrt{s} = 13$ TeV*, *JHEP* **04** (2019) 112 [[1810.11854](#)].
- [14] ATLAS collaboration, *Search for the $HH \rightarrow b\bar{b}b\bar{b}$ process via vector-boson fusion production using proton-proton collisions at $\sqrt{s} = 13$ TeV with the ATLAS detector*, *JHEP* **07** (2020) 108 [[2001.05178](#)].
- [15] CMS collaboration, *Search for Higgs Boson Pair Production in the Four b Quark Final State in Proton-Proton Collisions at $s=13$ TeV*, *Phys. Rev. Lett.* **129** (2022) 081802 [[2202.09617](#)].
- [16] ATLAS collaboration, *Search for Higgs boson pair production in the $b\bar{b}b\bar{b}$ final state from pp collisions at $\sqrt{s} = 8$ TeV with the ATLAS detector*, *Eur. Phys. J. C* **75** (2015) 412 [[1506.00285](#)].
- [17] ATLAS collaboration, *Search for pair production of Higgs bosons in the $b\bar{b}b\bar{b}$ final state using proton-proton collisions at $\sqrt{s} = 13$ TeV with the ATLAS detector*, *Phys. Rev. D* **94** (2016) 052002 [[1606.04782](#)].
- [18] ATLAS collaboration, *Search for pair production of Higgs bosons in the $b\bar{b}b\bar{b}$ final state using proton-proton collisions at $\sqrt{s} = 13$ TeV with the ATLAS detector*, *JHEP* **01** (2019) 030 [[1804.06174](#)].

- [19] CMS collaboration, *A portrait of the Higgs boson by the CMS experiment ten years after the discovery.*, *Nature* **607** (2022) 60 [2207.00043].
- [20] ATLAS collaboration, *Search for resonant pair production of Higgs bosons in the $b\bar{b}b\bar{b}$ final state using pp collisions at $\sqrt{s} = 13$ TeV with the ATLAS detector*, *Phys. Rev. D* **105** (2022) 092002 [2202.07288].
- [21] ATLAS collaboration, *Combination of searches for Higgs boson pair production in pp collisions at $\sqrt{s} = 13$ TeV with the ATLAS detector*, *Phys. Rev. Lett.* **133** (2024) 101801 [2406.09971].
- [22] CMS collaboration, *Combination of searches for nonresonant Higgs boson pair production in proton-proton collisions at $\sqrt{s} = 13$ TeV*, CMS Physics Analysis Summary **CMS-PAS-HIG-20-011** (2024).
- [23] A. Shmakov, M.J. Fenton, T.-W. Ho, S.-C. Hsu, D. Whiteson and P. Baldi, *SPANet: Generalized permutationless set assignment for particle physics using symmetry preserving attention*, *SciPost Phys.* **12** (2022) 178 [2106.03898].
- [24] M.J. Fenton, A. Shmakov, T.-W. Ho, S.-C. Hsu, D. Whiteson and P. Baldi, *Permutationless many-jet event reconstruction with symmetry preserving attention networks*, *Phys. Rev. D* **105** (2022) 112008 [2010.09206].
- [25] M.J. Fenton, A. Shmakov, H. Okawa, Y. Li, K.-Y. Hsiao, S.-C. Hsu et al., *Reconstruction of unstable heavy particles using deep symmetry-preserving attention networks*, *Commun. Phys.* **7** (2024) 139 [2309.01886].
- [26] C.-W. Chiang, F.-Y. Hsieh, S.-C. Hsu and I. Low, *Deep learning to improve the sensitivity of Di-Higgs searches in the $4b$ channel*, *JHEP* **09** (2024) 139 [2401.14198].
- [27] J. Duarte, H. Li and M. Stamenkovic, *HHH, HH, and QCD events for boosted and resolved Higgs boson jet assignment*, 2024. 10.5281/zenodo.14277439.
- [28] J. Duarte, H. Li, M. Stamenkovic, I. kavoori, J. Mitić and C. Mikkelsen, “ucsd-hep-ex/hhh: v0.1.0.” <https://github.com/ucsd-hep-ex/hhh>, 2024. 10.5281/zenodo.14248961.
- [29] A. Shmakov, H. Li, and J. Duarte, “billy000400/spanet.” <https://github.com/billy000400/SPANet>, 2024.
- [30] J. Alwall, R. Frederix, S. Frixione, V. Hirschi, F. Maltoni, O. Mattelaer et al., *The automated computation of tree-level and next-to-leading order differential cross sections, and their matching to parton shower simulations*, *JHEP* **07** (2014) 079 [1405.0301].
- [31] A. Papaefstathiou, T. Robens and G. Tetlalmatzi-Xolocotzi, *Triple Higgs Boson Production at the Large Hadron Collider with Two Real Singlet Scalars*, *JHEP* **05** (2021) 193 [2101.00037].
- [32] T. Sjöstrand, S. Ask, J.R. Christiansen, R. Corke, N. Desai, P. Ilten et al., *An Introduction to PYTHIA 8.2*, *Comput. Phys. Commun.* **191** (2015) 159 [1410.3012].
- [33] DELPHES 3 collaboration, *DELPHES 3, A modular framework for fast simulation of a generic collider experiment*, *JHEP* **02** (2014) 057 [1307.6346].
- [34] M. Cacciari, G.P. Salam and G. Soyez, *The anti- k_T jet clustering algorithm*, *JHEP* **04** (2008) 063 [0802.1189].
- [35] M. Cacciari, G.P. Salam and G. Soyez, *FastJet user manual*, *Eur. Phys. J. C* **72** (2012) 1896 [1111.6097].

- [36] CMS collaboration, *Identification of b-Quark Jets with the CMS Experiment*, *JINST* **8** (2013) P04013 [[1211.4462](#)].
- [37] S. Mondal and L. Mastrolorenzo, *Machine learning in high energy physics: a review of heavy-flavor jet tagging at the LHC*, *Eur. Phys. J. ST* **233** (2024) 2657 [[2404.01071](#)].
- [38] S.S. Snyder, *Measurement of the Top Quark Mass at D0*, Ph.D. thesis, SUNY, Stony Brook, 1995. [10.2172/1422822](#).
- [39] A.J. Larkoski, S. Marzani, G. Soyez and J. Thaler, *Soft Drop*, *JHEP* **05** (2014) 146 [[1402.2657](#)].
- [40] J. Thaler and K. Van Tilburg, *Identifying Boosted Objects with N-subjettiness*, *JHEP* **03** (2011) 015 [[1011.2268](#)].
- [41] A. Vaswani, N. Shazeer, N. Parmar, J. Uszkoreit, L. Jones, A.N. Gomez et al., *Attention is all you need*, in *Advances in Neural Information Processing Systems*, I. Guyon, U.V. Luxburg, S. Bengio, H. Wallach, R. Fergus, S. Vishwanathan et al., eds., vol. 30, p. 5998, Curran Associates, Inc., 2017, <http://papers.nips.cc/paper/7181-attention-is-all-you-need.pdf> [[1706.03762](#)].